

See discussions, stats, and author profiles for this publication at: <https://www.researchgate.net/publication/281585402>

CH₃NH₃PbI₃ and CH₃NH₃PbI₃-xCl_x in Planar or Mesoporous Perovskite Solar Cells: Comprehensive Insight into the Dependence of Performance on Architecture

ARTICLE in THE JOURNAL OF PHYSICAL CHEMISTRY C · JULY 2015

Impact Factor: 4.77 · DOI: 10.1021/acs.jpcc.5b02784

CITATION

1

READS

51

10 AUTHORS, INCLUDING:



Yantao Shi

Dalian University of Technology

52 PUBLICATIONS 454 CITATIONS

SEE PROFILE



Yu Li

Peking University

21 PUBLICATIONS 35 CITATIONS

SEE PROFILE



Shufeng Wang

Peking University

122 PUBLICATIONS 1,599 CITATIONS

SEE PROFILE



Tingli Ma

Dalian University of Technology

142 PUBLICATIONS 3,976 CITATIONS

SEE PROFILE

CH₃NH₃PbI₃ and CH₃NH₃PbI_{3-x}Cl_x in Planar or Mesoporous Perovskite Solar Cells: Comprehensive Insight into the Dependence of Performance on Architecture

Yantao Shi,^{*,†} Yujin Xing,[†] Yu Li,[‡] Qingshun Dong,[†] Kai Wang,[†] Yi Du,[†] Xiaogong Bai,[†] Shufeng Wang,[‡] Zhijian Chen,[‡] and Tingli Ma^{*,§,||}

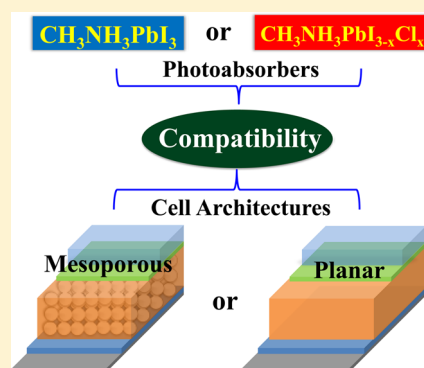
[†]State Key Laboratory of Fine Chemicals, School of Chemistry, Dalian University of Technology, Dalian 116012, P. R. China

[‡]Department of Physics, Peking University, Beijing 100871, P. R. China

[§]School of Petroleum and Chemical Engineering, Dalian University of Technology, Panjin 124221, P. R. China

^{||}Graduate School of Life Science and Systems Engineering, Kyushu Institute of Technology, Kitakyushu, Fukuoka 808-0196, Japan

ABSTRACT: In perovskite solar cells (PSCs), issues of compatibility between the photoabsorber and the cell architecture arise. In this work, we systematically demonstrated the characteristics of PSCs with an organometal halide, CH₃NH₃PbI₃ or CH₃NH₃PbI_{3-x}Cl_x, in a planar or mesoporous architecture, and the dependence of the cell photovoltaic performance on the architecture was illustrated in detail. In addition to the inherent photoelectric characteristics, CH₃NH₃PbI₃ and CH₃NH₃PbI_{3-x}Cl_x also differ in other aspects, such as light absorption, crystallinity, surface coverage, and dissociation of the photogenerated electrons. For PSCs with CH₃NH₃PbI₃, the mesoporous ones gave high power conversion efficiencies (PCE) of up to 14.05%, which is much higher than those of the planar ones (up to 6.76%). For PSCs with CH₃NH₃PbI_{3-x}Cl_x, the planar and mesoporous devices exhibited PCEs of up to 12.67% and 7.87%, respectively, quite in contrast with the case of CH₃NH₃PbI₃.



1. INTRODUCTION

In the past two years, organometal halide perovskites have emerged as novel photovoltaic materials with high carrier mobility, modest band gap, good solubility, and ambipolar behavior.^{1,2} These fascinating properties allow these materials to serve as good photoabsorbers and superior charge transport media for both electrons and holes.^{3,4} Despite many research efforts, the unsatisfactory power conversion efficiencies (PCEs) of 3–6% and rapidly declining performance because of ease of dissolution eventually made it infeasible to use CH₃NH₃PbI₃ nanocrystals as sensitizers in traditional dye-sensitized solar cells (DSCs).^{5,6} In 2012, by using a more rational design of the cell architecture, the groups of Grätzel and Park jointly reported a high PCE of 9.7% from the first all-solid-state and thin-film perovskite solar cells (PSCs) in which the mesoporous TiO₂ film loaded with CH₃NH₃PbI₃ nanocrystals was less than 1 μm in thickness and largely reduced compared with that in the DSCs.⁷ Moreover, the photogenerated electrons and holes in these primary PSCs were transported by mesoporous TiO₂ and spiro-OMeTAD, respectively. Shortly after the above-mentioned study on CH₃NH₃PbI₃ was conducted, Snaith and co-workers⁴ successfully introduced another perovskite, the mixed halide CH₃NH₃PbI_{3-x}Cl_x, into PSCs and achieved a high PCE of 10.9%. In this meso-superstructured solar cell (MSSC), CH₃NH₃PbI_{3-x}Cl_x was believed to be responsible for electron transport, whereas the mesoporous Al₂O₃ served as a scaffold layer only. Subsequently, PSCs were still able to work as usual

even in the absence of a hole conductor.^{8,9} In addition, planar PSCs with a perovskite photoabsorber sandwiched between two charge-selective layers could also generate high efficiencies.^{10,11}

The excellent properties of organometal halide perovskites render more flexibility to PSCs in architecture design. As of this writing, by means of various optimizations, both mesoporous and planar PSCs have exhibited high PCEs of up to 19%.^{12,13} As two of the most commonly used photoabsorbers in PSCs, CH₃NH₃PbI₃ and CH₃NH₃PbI_{3-x}Cl_x have been illustrated with different photoelectric characteristics, among which the most striking one is the electron–hole diffusion length. The electron–hole diffusion length is greater than 1 μm for CH₃NH₃PbI_{3-x}Cl_x, whereas in the case of CH₃NH₃PbI₃, it is only ca. 100 nm (according to the report by Stranks et al.¹⁴). Therefore, we can understand that when CH₃NH₃PbI_{3-x}Cl_x is used as a photoabsorber, planar PSCs and those with mesoporous Al₂O₃ scaffold layers both perform well because the photoinduced carriers can be separated as effectively as possible. However, PSCs with CH₃NH₃PbI_{3-x}Cl_x usually give relatively lower conversion efficiencies when combined with mesoscopic TiO₂ (m-TiO₂), thereby suggesting an incompatibility in the cell architecture.⁴ As of this writing, a PCE of over

Received: March 23, 2015

Revised: June 11, 2015

Published: June 22, 2015

12% has never been reported for PSCs based on $\text{CH}_3\text{NH}_3\text{PbI}_{3-x}\text{Cl}_x$ and m-TiO_2 . On the contrary, to achieve high efficiencies, most $\text{CH}_3\text{NH}_3\text{PbI}_3$ -based PSCs are fabricated by incorporating m-TiO_2 . Jeon and co-workers reportedly produced PSCs based on this cell architecture with high PCEs of up to 16.7%.¹⁵

Researchers have focused on the issue of compatibility between the photoabsorber and the cell architecture. Using electron-beam-induced current, Edri et al.¹⁶ compared PSCs based on the two typical photoabsorbers and concluded that m-TiO_2 (an electron conductor) is required in $\text{CH}_3\text{NH}_3\text{PbI}_3$ -based PSCs because holes can be extracted more efficiently than electrons. Meanwhile, in $\text{CH}_3\text{NH}_3\text{PbI}_{3-x}\text{Cl}_x$ -based PSCs, the effective diffusion lengths of electrons and holes are comparable, and therefore, m-TiO_2 is unnecessary. Currently, individual investigations on $\text{CH}_3\text{NH}_3\text{PbI}_3$ or $\text{CH}_3\text{NH}_3\text{PbI}_{3-x}\text{Cl}_x$ in PSCs have been performed intensively, whereas systematic comparisons have seldom been reported. In this work, we systematically demonstrated the characteristics of PSCs with $\text{CH}_3\text{NH}_3\text{PbI}_3$ or $\text{CH}_3\text{NH}_3\text{PbI}_{3-x}\text{Cl}_x$ as the photoabsorber and with planar or mesoporous architecture. The dependence of the cell photovoltaic performance on the architecture was illustrated in detail. In addition to the inherent photoelectric characteristics, $\text{CH}_3\text{NH}_3\text{PbI}_3$ and $\text{CH}_3\text{NH}_3\text{PbI}_{3-x}\text{Cl}_x$ also differ significantly in other aspects, such as light absorption, crystallinity, and surface coverage. For PSCs with $\text{CH}_3\text{NH}_3\text{PbI}_3$, the mesoporous one gave a high PCE of 14.05%, which was much higher than that from the planar one (6.76%). For PSCs with $\text{CH}_3\text{NH}_3\text{PbI}_{3-x}\text{Cl}_x$, the planar and the mesoporous ones exhibited PCEs of 12.67% and 7.87%, respectively, which were quite in contrast with the case of $\text{CH}_3\text{NH}_3\text{PbI}_3$.

2. EXPERIMENTAL SECTION

2.1. Fabrication of PSCs. According to previous works, fluorine-doped tin oxide (FTO)-coated glass ($15\ \Omega\ \text{sq}^{-1}$) was patterned by etching with Zn powder and 4 M hydrochloric acid, cleaning with a 2% Hellmanex solution, rinsing with deionized water, acetone, and isopropanol, and finally drying in clean air. A thin compact anatase TiO_2 (cp- TiO_2) layer was formed through spin-coating of a TiO_2 organic sol onto the clean substrate at 3000 rpm for 30 s followed by sintering in a furnace at $450\ ^\circ\text{C}$ for 2 h. The organic sol for the TiO_2 compact layer was prepared according to previous literature.¹⁷ Then mesoporous TiO_2 layers were prepared by spin-coating of a commercial TiO_2 paste (Dyesol-18NRT, Dyesol) diluted in ethanol (2:7 w/w) at 5000 rpm for 30 s. After drying at $125\ ^\circ\text{C}$, the mesoporous TiO_2 films were gradually heated to $500\ ^\circ\text{C}$ and calcinated for 30 min. $\text{CH}_3\text{NH}_3\text{PbI}_3$ -based PSCs were fabricated through sequential deposition. For planar and mesoscopic cells, the substrate (with only a cp- TiO_2 layer or a mesoporous layer) was infiltrated with PbI_2 by spin-coating at 5000 rpm for 5 s and drying at $70\ ^\circ\text{C}$ for 30 min. After cooling to room temperature, the film was dipped in a solution of $\text{CH}_3\text{NH}_3\text{I}$ in 2-propanol ($10\ \text{mg mL}^{-1}$) for 60 s, rinsed with 2-propanol, and dried at $70\ ^\circ\text{C}$ for 30 min to form the crystallized $\text{CH}_3\text{NH}_3\text{PbI}_3$. For the fabrication of PSCs based on $\text{CH}_3\text{NH}_3\text{PbI}_{3-x}\text{Cl}_x$, a precursor solution of $\text{CH}_3\text{NH}_3\text{I}$ and PbCl_2 in anhydrous N,N -dimethylformamide (DMF) at a 3:1 molar ratio was initially prepared. Then $60\ \mu\text{L}$ of 20 wt % precursor solution was spread onto the substrate with only the cp- TiO_2 layer or mesoporous layer for subsequent spin-coating at 2000 rpm for 30 s and then at 3000 rpm for another 30 s.

The coated films were then placed on a hot plate set at $100\ ^\circ\text{C}$ for 45 min. By spin-coating at 3000 rpm for 30 s, $50\ \mu\text{L}$ of hole-transporting material was then deposited. The spin-coating formulation was prepared by dissolving 72.3 mg of 2,2',7,7'-tetrakis(N,N -di-*p*-methoxyphenylamine)-9,9'-spiro-bifluorene (spiro-OMeTAD), $28.8\ \mu\text{L}$ of 4-*tert*-butylpyridine, $17.5\ \mu\text{L}$ of a stock solution of $520\ \text{mg mL}^{-1}$ lithium bis-(trifluoromethylsulfonyl)imide in acetonitrile, and $29\ \mu\text{L}$ of a stock solution of $300\ \text{mg mL}^{-1}$ tris(2-(1*H*-pyrazol-1-yl)-4-*tert*-butylpyridine)cobalt(III) bis(trifluoromethylsulfonyl)imide in acetonitrile in 1 mL of chlorobenzene. Finally, $50\ \text{nm}$ Ag was thermally evaporated on top of the device to form the back contact. The active area of this electrode was fixed at $0.06\ \text{cm}^2$.

2.2. Characterization. The microscopic morphologies of the perovskite in PSCs and the device cross sections were characterized by scanning electron microscopy (SEM) using an FEI Quanta 450 microscope. The crystallinity of the perovskite was characterized by X-ray diffraction (XRD) on a Rigaku D/Max-2400 diffractometer. The UV-vis absorbance spectra of perovskites were measured with a Hewlett-Packard HP 8453 UV-vis spectrophotometer by deducting the background of the compact or mesoporous TiO_2 layer. Photocurrent–voltage (J – V) curves were measured under AM 1.5 $100\ \text{mW cm}^{-2}$ irradiation (PEC-L15, Peccell, Yokohama, Japan) using a Keithley 2601 digital source meter. Before the J – V measurements, the light intensity was calibrated with a standard crystalline silicon solar cell. Incident-photon-to-electron conversion efficiency (IPCE) values were recorded using the monochromatic light from a system made of a xenon lamp, a monochromator, and appropriate filters. The femtosecond time-resolved fluorescence spectra were recorded using a high-resolution streak camera system (Hamamatsu C10910). An amplified mode-locked Ti:sapphire laser system (Legend, Coherent) delivered $800\ \text{nm}$, 35 fs pulses with a repetition rate of 1 kHz. The laser beam was used to pump a two-stage optical parametric amplifier (Opera Solo, Coherent) to generate the pump beam. All of the samples were excited using $517\ \text{nm}$ light at room temperature with $135\ \text{nJ cm}^{-2}$ pulse^{−1} to eliminate unwanted nonlinear effects such as exciton–charge annihilation. The lifetimes were obtained by fitting the resulting curves with a biexponential decay function of the form

$$I(t) = A_1 \exp\left(-\frac{t}{\tau_1}\right) + A_2 \exp\left(-\frac{t}{\tau_2}\right)$$

3. RESULTS AND DISCUSSION

3.1. Morphology, Structure, and Photoabsorbance. In this work, four types of PSCs were fabricated and characterized. According to the cell architectures, they were designated as M- TiO_2 - $\text{CH}_3\text{NH}_3\text{PbI}_3$, P- TiO_2 - $\text{CH}_3\text{NH}_3\text{PbI}_3$, M- TiO_2 - $\text{CH}_3\text{NH}_3\text{PbI}_{3-x}\text{Cl}_x$, and P- TiO_2 - $\text{CH}_3\text{NH}_3\text{PbI}_{3-x}\text{Cl}_x$, in which “M” and “P” stand for “mesoporous” and “planar”, respectively. Figure 1 comprehensively demonstrates the microstructures of the mesoporous and planar PSCs based on $\text{CH}_3\text{NH}_3\text{PbI}_3$ and $\text{CH}_3\text{NH}_3\text{PbI}_{3-x}\text{Cl}_x$. First, all of the functional layers as well as the interfaces in our four types of PSCs were clearly illustrated in the cross-sectional SEM images in Figure 1a–d. $\text{CH}_3\text{NH}_3\text{PbI}_3$ was prepared on mesoporous or compact TiO_2 films by sequential deposition, and one universal route was used in this field.¹⁸ From the top-view SEM images shown in Figure 1a₁, a₂, b₁, b₂, both the mesoporous and planar PSCs were

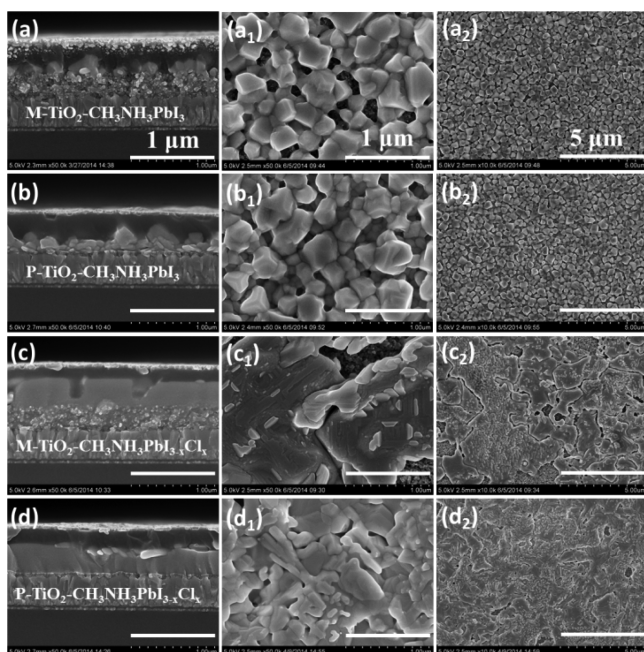


Figure 1. (a–d) Cross-sectional SEM images of various PSCs: (a) M-TiO₂-CH₃NH₃PbI₃; (b) P-TiO₂-CH₃NH₃PbI₃; (c) M-TiO₂-CH₃NH₃PbI_{3-x}Cl_x; (d) P-TiO₂-CH₃NH₃PbI_{3-x}Cl_x. Scale bars = 1 μm. (a₁–d₁, a₂–d₂) Corresponding top-view SEM images with different magnifications: (a₁–d₁) scale bars = 1 μm; (a₂–d₂) scale bars = 5 μm.

roughly covered by submicron crystals with nonuniform size distributions in the CH₃NH₃PbI₃-based devices. This morphological feature may have stemmed from inhomogeneous crystallization. On the contrary, in the mesoporous and planar devices, no evident difference in crystal sizes of CH₃NH₃PbI₃ was found on their top layers. Unlike CH₃NH₃PbI₃, the hybrid perovskite CH₃NH₃PbI_{3-x}Cl_x was prepared using the so-called “one-step” route via deposition of a mixed solution of CH₃NH₃I and PbCl₂ (at a mole ratio of 3:1).¹⁹ Figure 1c₁,c₂ and Figure 1d₁,d₂ show the top-view SEM images of the CH₃NH₃PbI_{3-x}Cl_x-based mesoporous and planar devices, respectively. Compared with those with CH₃NH₃PbI₃, the CH₃NH₃PbI_{3-x}Cl_x top layers have relatively flat surfaces and are also uniform in thickness, as shown in the cross-sectional SEM images in Figure 1c,d. However, there were some cracks in the CH₃NH₃PbI_{3-x}Cl_x-based mesoporous device, and the source was thought also to be related to inhomogeneous crystallization, including both nucleation and growth.

The crystallinity of the perovskites incorporated into mesoporous and planar cell architectures was characterized by XRD. As shown in Figure 2, the perovskite crystallized very well in the sample of M-TiO₂-CH₃NH₃PbI₃ despite a tiny peak ($2\theta = 12.65^\circ$) observed for crystallized PbI₂ that can be attributed to its (001) lattice plane. This finding has been intensively reported in published literature,^{20,21} suggesting that the incomplete conversion of PbI₂ into CH₃NH₃PbI₃ seems inevitable even though mesoporous TiO₂ could offer a large contact area for the interfacial reaction between PbI₂ and CH₃NH₃I. However, for the P-TiO₂-CH₃NH₃PbI₃ sample, the incomplete PbI₂ conversion was more pronounced because its characteristic peak was much stronger. By contrast, the diffraction peaks of CH₃NH₃PbI₃ were relatively weak. For the CH₃NH₃PbI_{3-x}Cl_x-based samples, neither PbI₂ nor PbCl₂

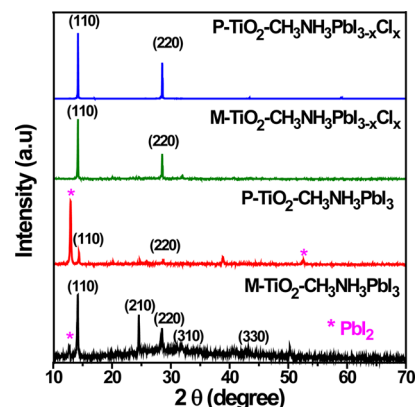


Figure 2. XRD patterns of M-TiO₂-CH₃NH₃PbI₃, P-TiO₂-CH₃NH₃PbI₃, M-TiO₂-CH₃NH₃PbI_{3-x}Cl_x, and P-TiO₂-CH₃NH₃PbI_{3-x}Cl_x fabricated by depositing perovskite on mesoporous (M) or planar (P) TiO₂ films.

peaks were found in the mesoporous and planar cells, indicating the good crystallinity of the iodide/chloride mixed-halide perovskite. This phenomenon is consistent with literature reports that chloride-containing halide perovskites are more easily crystallized.

The light-capturing capabilities of these samples were characterized by UV–vis absorption spectroscopy, as shown in Figure 3. Figure 3a indicates that across the range of visible

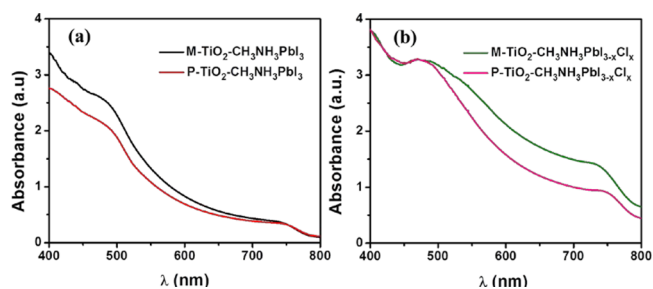


Figure 3. UV–vis absorbance spectra of (a) CH₃NH₃PbI₃ and (b) CH₃NH₃PbI_{3-x}Cl_x films deposited on compact or mesoporous TiO₂ films.

light (400 to 700 nm), the M-TiO₂-CH₃NH₃PbI₃ sample was superior to the one with the planar architecture. The better performance can be ascribed to the better crystallinity of the perovskite photoabsorber, and this finding is in good agreement with the XRD results. Although the two CH₃NH₃PbI_{3-x}Cl_x-based samples possessed good crystallinity, the one with mesoporous architecture obviously performed better than the planar one when the wavelength of the light was beyond 500 nm. This advantage probably came from the light-scattering effect of the TiO₂ mesoporous film.

3.2. Photovoltaic Performance. For the four types of PSCs with various configurations, Figure 4 presents the *J*–*V* curves of the respective champion devices measured under AM 1.5 100 mW cm^{−2} simulated light. The detailed photovoltaic parameters are summarized in Table 1. For the CH₃NH₃PbI₃-based PSCs, the one with the mesoporous configuration exhibited a much higher open-circuit voltage (*V*_{OC}), short-circuit current density (*J*_{SC}), and fill factor (FF) than the one with the planar configuration. Consequently, a PCE of 14.05% was obtained with the M-TiO₂-CH₃NH₃PbI₃ PSC, which is notably higher than the PCE of 6.76% for the P-TiO₂-

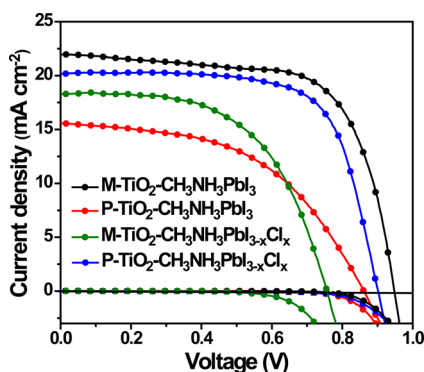


Figure 4. Current–voltage (J – V) curves for the champion PSCs of the four configuration types.

Table 1. Photovoltaic Parameters of the Champion PSCs for the Four Configuration Types

PSC	V_{OC} (V)	J_{SC} (mA cm^{-2})	FF (%)	PCE (%)
M-TiO ₂ –CH ₃ NH ₃ PbI ₃	0.95	21.96	0.67	14.05
P-TiO ₂ –CH ₃ NH ₃ PbI ₃	0.86	15.58	0.50	6.76
M-TiO ₂ –CH ₃ NH ₃ PbI _{3-x} Cl _x	0.76	18.28	0.57	7.87
P-TiO ₂ –CH ₃ NH ₃ PbI _{3-x} Cl _x	0.90	20.13	0.70	12.67

CH₃NH₃PbI₃ PSC. According to published works, P-TiO₂–CH₃NH₃PbI₃ PSCs have been inferior to M-TiO₂–CH₃NH₃PbI₃ PSCs for a long time. Although researchers in this field are inclined to ascribe this fact to the shorter electron diffusion length in CH₃NH₃PbI₃, we believe that the incomplete conversion to CH₃NH₃PbI₃ ought to be responsible for the lower PCE. Actually, as reported previously, sometimes the proper amount of residual PbI₂ in PSCs shows a positive effect on the PSC performance by suppressing charge recombination at the TiO₂–perovskite interface or grain boundaries of perovskite crystals.^{22,23} In contrast, in our work the amount of residual PbI₂ in the P-TiO₂–CH₃NH₃PbI₃ PSCs was very large, as confirmed by XRD results. Therefore, it would undoubtedly hinder the transport and collection of photogenerated electrons. In 2014, improving the crystallization of CH₃NH₃PbI₃ was shown to greatly promote the photovoltaic performance of P-TiO₂–CH₃NH₃PbI₃ PSCs, as reported by Wu et al.²⁴ and Xiao et al.²⁵ However, for the CH₃NH₃PbI_{3-x}Cl_x-based PSCs, well-crystallized perovskite has been incorporated into the two configurations, but differences in the photovoltaic performances of the M-TiO₂–CH₃NH₃PbI_{3-x}Cl_x and P-TiO₂–CH₃NH₃PbI_{3-x}Cl_x PSCs are noted. In addition, M-TiO₂–CH₃NH₃PbI_{3-x}Cl_x PSCs are evidently inferior to P-TiO₂–CH₃NH₃PbI_{3-x}Cl_x PSCs in CH₃NH₃PbI_{3-x}Cl_x-based devices. As shown in Table 1, the V_{OC} , J_{SC} , and FF for P-TiO₂–CH₃NH₃PbI_{3-x}Cl_x PSCs were 0.90 V, 20.13 mA cm^{-2} , and 0.70, respectively, resulting in a PCE of 12.67%. By contrast, because of the lower V_{OC} , J_{SC} , and FF, the PCE of M-TiO₂–CH₃NH₃PbI_{3-x}Cl_x PSCs was only 7.87%.

As the photoabsorber in PSCs, CH₃NH₃PbI_{3-x}Cl_x performed better with the mesoporous architecture than with the planar one. In general, better light absorption leads to a higher efficiency, at least a higher photocurrent. However, the fact that both the J_{SC} and PCE of the M-TiO₂–CH₃NH₃PbI_{3-x}Cl_x device were lower than those of the P-TiO₂–CH₃NH₃PbI_{3-x}Cl_x device indicated that it was the charge

diffusion or recombination that finally determined the photovoltaic performance. Actually, it has been reported that CH₃NH₃PbI_{3-x}Cl_x performs better in planar cells because the intrinsic diffusion length of the two types of carriers (electron and hole) are comparable.^{16,26} Hence, the introduction of mesoporous TiO₂ into CH₃NH₃PbI_{3-x}Cl_x-based PSCs does not contribute significantly to the transport and collection of electrons. Instead, the negative effect of mesoporous TiO₂ would be more pronounced because it would introduce massive surface states while largely extending the interfacial area, which in turn would enhance the probability of charge recombination. The dark current in M-TiO₂–CH₃NH₃PbI_{3-x}Cl_x PSCs was larger than that in P-TiO₂–CH₃NH₃PbI_{3-x}Cl_x PSCs. Moreover, for each type of PSC, 30 individual devices were fabricated to evaluate the reproducibility of the photovoltaic performance. First, M-TiO₂–CH₃NH₃PbI₃ and P-TiO₂–CH₃NH₃PbI_{3-x}Cl_x PSCs were generally able to give higher PCEs than the other two types of PSCs, as shown in Figure 5.

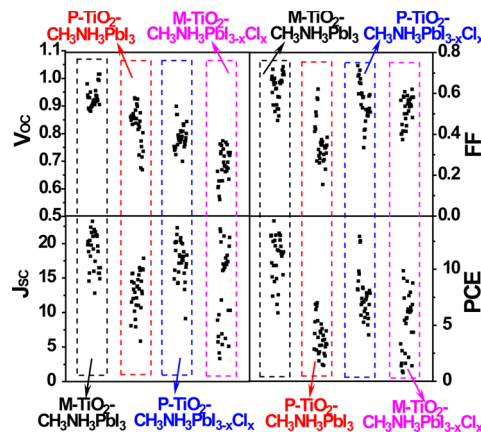


Figure 5. Diagram of the photovoltaic parameter distributions of the four types of PSCs.

However, the reproducibility for each type of PSC was not very satisfactory, which can be ascribed to the difficulties in realizing full conversion of PbI₂ and effective control of the perovskite crystal size and surface morphology. Thus, accurate control and development of more advanced technology in fabrication are urgent and necessary. For example, the use of dimethyl sulfoxide instead of DMF in the sequential deposition of the perovskite layer overcame the above problems, and subsequently, the reproducibility of the PSCs was enhanced remarkably.²⁴ For the one-step method, Liang et al.²⁷ incorporated one specific additive into the perovskite precursor solution. It was found that homogeneous nucleation was obviously facilitated through the chelation effect with Pb²⁺, which in turn largely modulated the perovskite surface morphology and enhanced the cell performance.

3.3. External Quantum Efficiency and Interfacial Charge Extraction. The IPCE spectra and the integrated photocurrent densities of the four types of PSCs, shown in Figure 6, are in good agreement with the photocurrents illustrated in the J – V curves. Aside from the P-TiO₂–CH₃NH₃PbI₃ PSCs, the other three exhibited external quantum efficiencies exceeding 80%, as illustrated in Figure 6a. The IPCE profile for M-TiO₂–CH₃NH₃PbI_{3-x}Cl_x PSCs was somewhat different from those for the other two efficient PSCs. In detail, the maximum value of its IPCE appeared in the range of 340–370 nm, and then a sharp decrease followed as the wavelength

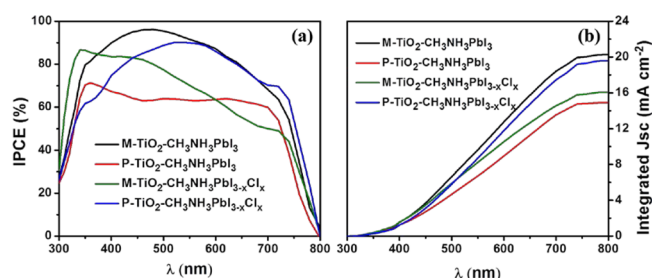


Figure 6. (a) IPCE and (b) integrated J_{SC} curves for $\text{CH}_3\text{NH}_3\text{PbI}_3$ - and $\text{CH}_3\text{NH}_3\text{PbI}_{3-x}\text{Cl}_x$ -based mesoporous and planar PSCs.

was extended to visible light. By contrast, broad and efficient photoelectric conversion covering the whole range of visible light can be observed for both $\text{P-TiO}_2\text{-CH}_3\text{NH}_3\text{PbI}_{3-x}\text{Cl}_x$ and $\text{M-TiO}_2\text{-CH}_3\text{NH}_3\text{PbI}_3$. In addition to strong light absorption, efficient dissociation of the photogenerated electrons was also of great significance in obtaining highly efficient solar cells. In this work, we also evaluated the charge dissociation by means of time-resolved photoluminescence (PL) quenching measurements. Details of the sample fabrication and measurement can be found in the Experimental Section. For each sample, the PL lifetimes were obtained by fitting the spectra using a biexponential decay function that contained fast decay (τ_1) and slow decay (τ_2) processes. In general, the fast decay might have originated from the quenching of free electrons in the perovskite through the transport to TiO_2 , whereas the slow process could be the result of radiative decay. Figure 7

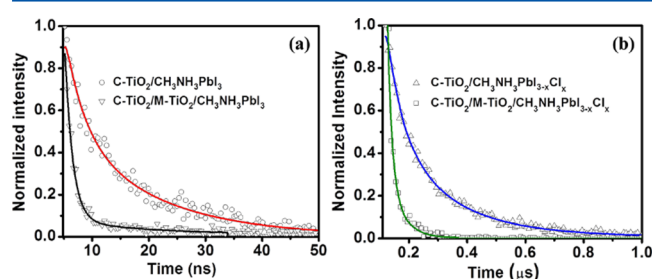


Figure 7. Time-resolved PL measurements on (a) $\text{CH}_3\text{NH}_3\text{PbI}_3$ - and (b) $\text{CH}_3\text{NH}_3\text{PbI}_{3-x}\text{Cl}_x$ -based samples with planar or mesoporous configurations.

demonstrates the PL decay, and the fitting results are summarized in Table 2, from which we can initially see that the time scale for the $\text{CH}_3\text{NH}_3\text{PbI}_3$ -based sample was in nanoseconds. As far as the fast decay ($\tau_1 \approx 3.34$ ns) is concerned, a weight fraction of 48% was observed for the $\text{FTO/cp-TiO}_2/\text{CH}_3\text{NH}_3\text{PbI}_3$ sample. By contrast, the $\text{FTO/cp-TiO}_2/\text{m-TiO}_2/\text{CH}_3\text{NH}_3\text{PbI}_3$ sample exhibited a much faster decay ($\tau_1 \approx 1.34$ ns). Meanwhile, the fraction of fast decay increased drastically to 94%, indicating that the mesoporous TiO_2 framework can enable much faster and more efficient dissociation of photogenerated electrons by providing a large

interfacial contact area. For $\text{CH}_3\text{NH}_3\text{PbI}_{3-x}\text{Cl}_x$ -based samples, the time scale for the PL decay was in microseconds. On the contrary, incorporation of the mesoporous TiO_2 decreased the fraction of fast decay from 52% to 23%. This finding suggests that mesoporous TiO_2 is incompatible with $\text{CH}_3\text{NH}_3\text{PbI}_{3-x}\text{Cl}_x$ -based PSCs because TiO_2 would hinder the dissociation of the photogenerated electrons.

4. CONCLUSIONS

We systematically compared the characteristics of four types of PSCs having either $\text{CH}_3\text{NH}_3\text{PbI}_3$ or $\text{CH}_3\text{NH}_3\text{PbI}_{3-x}\text{Cl}_x$ as the photoabsorber and either a planar or mesoporous architecture. These characteristics included light absorption, perovskite crystallinity, surface coverage, electron dissociation, and photovoltaic performance. With these characteristics, the compatibility between photoabsorber and cell architecture was well illustrated. For $\text{CH}_3\text{NH}_3\text{PbI}_3$ -based PSCs, the mesoporous cell showed better performance. The use of the TiO_2 mesoporous layer enabled the efficient crystallization of perovskite and electron injection because it can provide a large interfacial contact area. However, for the $\text{CH}_3\text{NH}_3\text{PbI}_{3-x}\text{Cl}_x$ -based PSCs, the mesoporous TiO_2 was observed to be unfavorable for the dissociation of the photogenerated electrons. For PSCs with $\text{CH}_3\text{NH}_3\text{PbI}_3$, the mesoporous ones gave high PCEs of up to 14.05%, which is much higher than those of up to 6.76% for the planar ones. For PSCs with $\text{CH}_3\text{NH}_3\text{PbI}_{3-x}\text{Cl}_x$, the planar and mesoporous devices exhibited PCEs as high as 12.67% and 7.87%, respectively, and such results were the opposite of those obtained for $\text{CH}_3\text{NH}_3\text{PbI}_3$.

AUTHOR INFORMATION

Corresponding Authors

*Y.S.: Tel: +86-411-84986237. E-mail: shiyantao@dlut.edu.cn.

*T.M.: Tel: +86-411-84986237. E-mail: tinglima@dlut.edu.cn.

Notes

The authors declare no competing financial interest.

ACKNOWLEDGMENTS

This work was financially supported by the National Natural Science Foundation of China (Grants 51402036, 51273032, and 91333104), the International Science & Technology Cooperation Program of China (Grant 2013DFA51000), and the Fundamental Research Funds for the Central Universities (Grant DUT15YQ109).

REFERENCES

- (1) Stoumpos, C. C.; Malliakas, C. D.; Kanatzidis, M. G. Semiconducting Tin and Lead Iodide Perovskites with Organic Cations: Phase Transitions, High Mobilities, and Near-Infrared Photoluminescent Properties. *Inorg. Chem.* **2013**, *52*, 9019–9038.
- (2) Noh, J. H.; Im, S. H.; Heo, J. H.; Mandal, T. N.; Seok, S. I. Chemical Management for Colorful, Efficient, and Stable Inorganic–

Table 2. Fitting Results of the PL Measurements

sample configuration	τ_1	fraction 1	τ_2	fraction 2
FTO/cp-TiO ₂ /CH ₃ NH ₃ PbI ₃	3.34 ± 0.36 ns	48%	15.36 ± 0.36 ns	52%
FTO/cp-TiO ₂ /m-TiO ₂ /CH ₃ NH ₃ PbI ₃	1.34 ± 0.06 ns	94%	14.24 ± 1.24 ns	6%
FTO/cp-TiO ₂ /CH ₃ NH ₃ PbI _{3-x} Cl _x	0.06 ± 0.005 μs	52%	0.21 ± 0.004 μs	48%
FTO/cp-TiO ₂ /m-TiO ₂ /CH ₃ NH ₃ PbI _{3-x} Cl _x	0.04 ± 0.001 μs	23%	0.01 ± 0.0006 μs	77%

Organic Hybrid Nanostructured Solar Cells. *Nano Lett.* **2013**, *13*, 1764–1769.

(3) Chung, I.; Lee, B.; He, J. Q.; Chang, R. P. H.; Kanatzidis, M. G. All-Solid-State Dye-Sensitized Solar Cells with High Efficiency. *Nature* **2012**, *485*, 486–489.

(4) Lee, M. M.; Teuscher, J.; Miyasaka, T.; Murakami, T. N.; Snaith, H. J. Efficient Hybrid Solar Cells Based on Meso-Superstructured Organometal Halide Perovskites. *Science* **2012**, *338*, 643–647.

(5) Kojima, A.; Teshima, K.; Shirai, Y.; Miyasaka, T. Organometal Halide Perovskites as Visible-Light Sensitizers for Photovoltaic Cells. *J. Am. Chem. Soc.* **2009**, *131*, 6050–6051.

(6) Im, J. H.; Lee, C. R.; Lee, J. W.; Park, S. W.; Park, N. G. 6.5% Efficient Perovskite Quantum-Dot-Sensitized Solar Cell. *Nanoscale* **2011**, *3*, 4088–4093.

(7) Kim, H.-S.; Lee, C.-R.; Im, J.-H.; Lee, K.-B.; Moehl, T.; Marchioro, A.; Moon, S.-J.; Humphry-Baker, R.; Yum, J.-H.; Moser, J. E.; Grätzel, M.; Park, N.-G. Lead Iodide Perovskite Sensitized All-Solid-State Submicron Thin Film Mesoscopic Solar Cell with Efficiency Exceeding 9%. *Sci. Rep.* **2012**, *2*, No. 591.

(8) Etgar, L.; Gao, P.; Xue, Z. S.; Peng, Q.; Chandiran, A. K.; Liu, B.; Nazeeruddin, M. K.; Grätzel, M. Mesoscopic $\text{CH}_3\text{NH}_3\text{PbI}_3/\text{TiO}_2$ Heterojunction Solar Cells. *J. Am. Chem. Soc.* **2012**, *134*, 17396–17399.

(9) Abu Laban, W.; Etgar, L. Depleted Hole Conductor-Free Lead Halide Iodide Heterojunction Solar Cells. *Energy Environ. Sci.* **2013**, *6*, 3249–3253.

(10) Chen, Q.; Zhou, H.; Hong, Z.; Luo, S.; Duan, H.-S.; Wang, H.-H.; Liu, Y.; Li, G.; Yang, Y. Planar Heterojunction Perovskite Solar Cells via Vapor-Assisted Solution Process. *J. Am. Chem. Soc.* **2014**, *136*, 622–625.

(11) Liu, M. Z.; Johnston, M. B.; Snaith, H. J. Efficient Planar Heterojunction Perovskite Solar Cells by Vapour Deposition. *Nature* **2013**, *501*, 395–398.

(12) Zhou, H. P.; Chen, Q.; Li, G.; Luo, S.; Song, T. B.; Duan, H. S.; Hong, Z. R.; You, J. B.; Liu, Y. S.; Yang, Y. Interface Engineering of Highly Efficient Perovskite Solar Cells. *Science* **2014**, *345*, 542–546.

(13) Jeon, N. J.; Noh, J. H.; Yang, W. S.; Kim, Y. C.; Ryu, S.; Seo, J.; Seok, S. I. Compositional Engineering of Perovskite Materials for High-Performance Solar Cells. *Nature* **2015**, *517*, 476–480.

(14) Stranks, S. D.; Eperon, G. E.; Grancini, G.; Menelaou, C.; Alcocer, M. J. P.; Leijtens, T.; Herz, L. M.; Petrozza, A.; Snaith, H. J. Electron–Hole Diffusion Lengths Exceeding 1 Micrometer in an Organometal Trihalide Perovskite Absorber. *Science* **2013**, *342*, 341–344.

(15) Jeon, N. J.; Lee, H. G.; Kim, Y. C.; Seo, J.; Noh, J. H.; Lee, J.; Seok, S. I. O-Methoxy Substituents in Spiro-OMeTAD for Efficient Inorganic–Organic Hybrid Perovskite Solar Cells. *J. Am. Chem. Soc.* **2014**, *136*, 7837–7840.

(16) Edri, E.; Kirmayer, S.; Henning, A.; Mukhopadhyay, S.; Gartsman, K.; Rosenwaks, Y.; Hodes, G.; Cahen, D. Why Lead Methylammonium Tri-Iodide Perovskite-Based Solar Cells Require a Mesoporous Electron Transporting Scaffold (but Not Necessarily a Hole Conductor). *Nano Lett.* **2014**, *14*, 1000–1004.

(17) Yu, H.; Zhang, S. Q.; Zhao, H. J.; Xue, B. F.; Liu, P. R.; Will, G. High-Performance TiO_2 Photoanode with an Efficient Electron Transport Network for Dye-Sensitized Solar Cells. *J. Phys. Chem. C* **2009**, *113*, 16277–16282.

(18) Burschka, J.; Pellet, N.; Moon, S.-J.; Humphry-Baker, R.; Gao, P.; Nazeeruddin, M. K.; Grätzel, M. Sequential Deposition as a Route to High-Performance Perovskite-Sensitized Solar Cells. *Nature* **2013**, *499*, 316–319.

(19) Eperon, G. E.; Burlakov, V. M.; Docampo, P.; Goriely, A.; Snaith, H. J. Morphological Control for High Performance, Solution-Processed Planar Heterojunction Perovskite Solar Cells. *Adv. Funct. Mater.* **2014**, *24*, 151–157.

(20) Dualeh, A.; Tetreault, N.; Moehl, T.; Gao, P.; Nazeeruddin, M. K.; Grätzel, M. Effect of Annealing Temperature on Film Morphology of Organic–Inorganic Hybrid Perovskite Solid-State Solar Cells. *Adv. Funct. Mater.* **2014**, *24*, 3250–3258.

(21) Wang, L. L.; McCleese, C.; Kovalsky, A.; Zhao, Y. X.; Burda, C. Femtosecond Time-Resolved Transient Absorption Spectroscopy of $\text{CH}_3\text{NH}_3\text{PbI}_3$ Perovskite Films: Evidence for Passivation Effect of PbI_2 . *J. Am. Chem. Soc.* **2014**, *136*, 12205–12208.

(22) Cao, D. H.; Stoumpos, C. C.; Malliakas, C. D.; Katz, M. J.; Farha, O. K.; Hupp, J. T.; Kanatzidis, M. G. Remnant PbI_2 , an Unforeseen Necessity in High-Efficiency Hybrid Perovskite-Based Solar Cells? *Appl. Mater.* **2014**, *2*, No. 091101.

(23) Chen, Q.; Zhou, H.; Song, T.-B.; Luo, S.; Hong, Z.; Duan, H.-S.; Dou, L.; Liu, Y.; Yang, Y. Controllable Self-Induced Passivation of Hybrid Lead Iodide Perovskites toward High Performance Solar Cells. *Nano Lett.* **2014**, *14*, 4158–4163.

(24) Wu, Y. Z.; Islam, A.; Yang, X. D.; Qin, C. J.; Liu, J.; Zhang, K.; Peng, W. Q.; Han, L. Y. Retarding the Crystallization of PbI_2 for Highly Reproducible Planar-Structured Perovskite Solar Cells via Sequential Deposition. *Energy Environ. Sci.* **2014**, *7*, 2934–2938.

(25) Xiao, Z. G.; Dong, Q. F.; Bi, C.; Shao, Y. C.; Yuan, Y. B.; Huang, J. S. Solvent Annealing of Perovskite-Induced Crystal Growth for Photovoltaic-Device Efficiency Enhancement. *Adv. Mater.* **2014**, *26*, 6503–6509.

(26) Xing, G.; Mathews, N.; Sun, S.; Lim, S. S.; Lam, Y. M.; Grätzel, M.; Mhaisalkar, S.; Sum, T. C. Long-Range Balanced Electron- and Hole-Transport Lengths in Organic–Inorganic $\text{CH}_3\text{NH}_3\text{PbI}_3$. *Science* **2013**, *342*, 344–347.

(27) Liang, P.-W.; Liao, C.-Y.; Chueh, C.-C.; Zuo, F.; Williams, S. T.; Xin, X.-K.; Lin, J.; Jen, A. K. Y. Additive Enhanced Crystallization of Solution-Processed Perovskite for Highly Efficient Planar-Heterojunction Solar Cells. *Adv. Mater.* **2014**, *26*, 3748–3754.